

Spatial Covariance Modeling for Stochastic Subgrid-Scale Parameterizations Using Dynamic Mode Decomposition

Federica Gugole¹ and Christian Franzke¹

¹Meteorological Institute and Center for Earth System Research and Sustainability

November 24, 2022

Abstract

Stochastic parameterizations are broadly used in climate modeling to represent subgrid scale processes. While different parameterizations are being developed considering different aspects of the physical phenomena, less attention is given to the technical and numerical aspects. In particular, the use of Empirical Orthogonal Functions (EOFs) is well established whenever a spatial structure is required, without considering its possible drawbacks. By applying an energy consistent parameterization to the 2-layer Quasi-Geostrophic (QG) model, we investigate the model sensitivity to the *a priori* assumptions made on the parameterization. In particular, we consider here two methods to prescribe the spatial covariance of the noise. First, by using climatological variability patterns provided by EOFs, and second, by using time-varying dynamics-adapted Koopman modes, approximated by Dynamic Mode Decomposition (DMD). The performance of the two methods are analyzed through numerical simulations of the stochastic system on a coarse spatial resolution, and the outcomes compared to a high-resolution simulation of the original deterministic system. The comparison reveals that the DMD based noise covariance scheme outperforms the EOF based. The use of EOFs leads to a significant increase of the ensemble spread, and to a meridional misplacement of the bi-modal eddy kinetic energy (EKE) distribution. On the other hand, using DMDs, the ensemble spread is confined and the meridional propagation of the zonal jet stream is accurately captured. Our results highlight the importance of the systematic design of stochastic parameterizations with dynamically adapted spatial correlations, rather than relying on statistical spatial patterns.

Abstract

Stochastic parameterizations are broadly used in climate modeling to represent subgrid scale processes. While different parameterizations are being developed considering different aspects of the physical phenomena, less attention is given to the technical and numerical aspects. In particular, the use of Empirical Orthogonal Functions (EOFs) is well established whenever a spatial structure is required, without considering its possible drawbacks. By applying an energy consistent parameterization to the 2-layer Quasi-Geostrophic (QG) model, we investigate the model sensitivity to the *a priori* assumptions made on the parameterization. In particular, we consider here two methods to prescribe the spatial covariance of the noise. First, by using climatological variability patterns provided by EOFs, and second, by using time-varying dynamics-adapted Koopman modes, approximated by Dynamic Mode Decomposition (DMD). The performance of the two methods are analyzed through numerical simulations of the stochastic system on a coarse spatial resolution, and the outcomes compared to a high-resolution simulation of the original deterministic system. The comparison reveals that the DMD based noise covariance scheme outperforms the EOF based. The use of EOFs leads to a significant increase of the ensemble spread, and to a meridional misplacement of the bi-modal eddy kinetic energy (EKE) distribution. On the other hand, using DMDs, the ensemble spread is confined and the meridional propagation of the zonal jet stream is accurately captured. Our results highlight the importance of the systematic design of stochastic parameterizations with dynamically adapted spatial correlations, rather than relying on statistical spatial patterns.

1 Introduction

Geophysical flows involve a multitude of phenomena with vastly different spatial and temporal scales (e.g. Franzke, Oliver, Rademacher, & Badin, 2019; Vallis, 2006). Due to the underlying nonlinear equations of motion all these scales interact with each other. In order to obtain dynamically consistent and stable long time simulations, geophysical models need, in principle, to cover the whole range of scales. This poses great computational challenges: processes occurring on spatial scales smaller than the prescribed numerical grid scale and processes occurring on temporal scales faster than the prescribed numerical time step cannot be resolved. These unresolved subgrid-scale processes nevertheless may be energetically important, such as, for example, convection processes which are not resolved by current climate models, and may significantly affect the dynamics on the large resolved scales. To capture the effects of the subgrid-scale processes, parameterizations are typically introduced, whereby the unresolved scales are conditioned on the resolved scales (Stensrud, 2007).

Further complications, caused by the inevitable distinction between resolved and unresolved spatial scales, in numerical schemes occur for nonlinear fluid systems which exhibit energy and enstrophy cascades. For atmospheric dynamics it is well known that enstrophy is transferred from larger to smaller scales, until it is dissipated at the dissipation scale, whereas energy is transported from smaller to larger scales (Dubrulle, 2019; Vallis, 2006). For the majority of models, as for instance for general circulation models, the numerical resolution is not fine enough to resolve the dissipation processes. Subsequently, the enstrophy piles up at the truncation level, making the numerical model unstable and subject to numerical blow up. In order to guarantee numerical stability, artificial hyper-viscosity is introduced, leading to an increased viscosity of the fluid, which dissipates also the kinetic energy. Furthermore, the injection of energy from the unresolved subgrid-scales leads to an unphysical grid-size dependent representation of the kinetic energy.

In recent years there has been an extensive interest in the development of stochastic parameterizations for sub-grid scale processes (e.g. Berner et al., 2017; Franzke, O’Kane,

65 Berner, Williams, & Lucarini, 2015; Gottwald, Crommelin, & Franzke, 2017; Imkeller
 66 & von Storch, 2001; Palmer & Williams, 2010). To mitigate possible damaging effects
 67 on the predictability by artificial energy dissipation, there has been a growing interest
 68 in designing energy-conserving and energy-consistent stochastic parametrizations (e.g.
 69 Dwivedi, Franzke, & Lunkeit, 2019; Frank & Gottwald, 2013; Gugole & Franzke, 2019;
 70 Jansen & Held, 2014; Jansen, Held, Adcroft, & Hallberg, 2015; Mémin, 2014; Resseguier,
 71 Mémin, & Chapron, 2017b). Broadly speaking, energy-consistent parametrizations fall
 72 into two different categories. The first approach is to derive expressions for additional
 73 terms to augment current deterministic fluid equations, such as done for kinetic back-
 74 scatter (Dwivedi et al., 2019; Jansen & Held, 2014; Juricke, Danilov, Kutsenko, & Oliver,
 75 2019; Zurita-Gotor, Held, & Jansen, 2015). The second strategy is to instead derive new
 76 stochastic expressions of the geophysical flow equations such that they still conserve, for
 77 instance, energy (Mémin, 2014; Resseguier, Mémin, & Chapron, 2017a; Resseguier et al.,
 78 2017b; Resseguier, Pan, & Fox-Kemper, 2019) or the Kelvin circulation theorem (Cot-
 79 ter, Crisan, Holm, Pan, & Shevchenko, 2018, 2019; Cotter, Gottwald, & Holm, 2017; Holm,
 80 2015).

81 We consider here a forced and damped 2-layer Quasi-Geostrophic (QG) model, and
 82 as stochastic parameterization we employ the projection operator approach introduced
 83 in Frank and Gottwald (2013). The energy-consistent parametrization developed in Frank
 84 and Gottwald (2013) had been devised only for a low-dimensional Hamiltonian ordinary
 85 differential equation. Subsequently it was successfully adapted for an unforced inviscid
 86 QG model in Gugole and Franzke (2019). However, the spatial covariance of the stochas-
 87 tic parametrization is not specified by the methodology suggested in Frank and Gottwald
 88 (2013), and in Gugole and Franzke (2019) it was shown to be crucial for the system to
 89 have physically meaningful results. Our aim is to further investigate the sensitivity of
 90 the model dynamics with respect to the definition of the noise covariance. Such a noise
 91 covariance is usually determined *a priori* and is not representative of some specific scale-
 92 dynamics. Very often Empirical Orthogonal Functions (EOFs) (von Storch & Zwiers,
 93 2003)) are employed for this purpose.

94 In addition to using EOFs, which capture the climatological dominant patterns of
 95 the variability, we will investigate spatial covariances based on Dynamic Mode Decom-
 96 position (DMD) (Kutz, Brunton, Brunton, & Proctor, 2016; Schmid, 2010; Schmid, Li,
 97 Juniper, & Pust, 2011). DMD is a computationally cost-effective algorithm attempting
 98 to compute a finite-dimensional approximation of the Koopman operator. The infinite-
 99 dimensional Koopman operator encodes the dynamics of a dynamical system and prop-
 100 agates observables in time (Lasota & Mackey, 1994). The intimate relationship between
 101 DMD modes and the eigenfunctions of the Koopman operator was established in Row-
 102 ley, Mezić, Bagheri, Schlatter, and Henningson (2009). The patterns extracted by the
 103 DMD method, the so called DMD or Koopman modes, describe the dominant dynam-
 104 ical structures, and their corresponding eigenvalues characterize their temporal oscilla-
 105 tion periods and their growth rates. In contrast to EOFs, DMD decomposes the dynam-
 106 ics according to its local in time oscillatory behavior. Connections between DMD and
 107 other model reduction techniques such as EOF or linear inverse modeling are discussed
 108 in Penland (1989); Penland and Magorian (1993); Schmid et al. (2011); Tu, Rowley, Lucht-
 109 enburg, Brunton, and Kutz (2014). By projecting the full system onto the subspace spanned
 110 by the leading DMD modes, the governing equations may be approximated by a low-dimensional
 111 dynamical system allowing to study flow stability and bifurcations among other char-
 112 acteristics (Bagheri, 2013; Jovanovic, Schmid, & Nichols, 2014; Noack, Stankiewicz, Morzyaski,
 113 & Schmid, 2016; Schmid, 2010; Schmid et al., 2011; Schmid, Meyer, & Pust, 2009). Here
 114 we shall use DMDs to construct the spatial structure of the noise covariance matrix. DMDs
 115 have the same numerical complexity as EOFs, and have the advantage of using infor-
 116 mation of the system on the fly, with no additional information. For more details on DMDs
 117 and its limitations in approximating Koopman modes the interested reader is referred
 118 to Tu et al. (2014); Williams, Kevrekidis, and Rowley (2015)).

119 In contrast to approaches attempting to determine subgrid-scale information from
 120 highly resolved simulations (e.g. Berloff, 2005; Franzke, Majda, & Vanden-Eijnden, 2005;
 121 Hermanson, Hoskins, & Palmer, 2009; Porta Mana & Zanna, 2014), our approach us-
 122 ing DMDs has the potential to seamlessly adapt to any grid resolution and is, hence, scale-
 123 adaptive. Our results show that the use of a dynamically adapted noise covariance keeps
 124 the ensemble spread confined and the meridional propagation of the zonal jet is better
 125 captured than with EOFs.

126 The remainder of this paper is structured as follows: In Section 2 we introduce the
 127 forced and damped 2-layer QG model. Section 3 describes the energy-consistent stochas-
 128 tic parameterization scheme. The spatial covariance of the noise is determined in Sec-
 129 tion 4 using EOF and DMD analysis. Section 5 presents results from numerical simu-
 130 lations exploring the effect of employing either climatological or dynamically adapted
 131 spatial covariances. We conclude with a discussion in Section 6.

132 2 The QG model

133 We consider the non-dimensional forced and damped 2-layer QG equations on a
 134 β -plane with double periodic boundary conditions (Vallis, 2006). This model represents
 135 synoptic-scale atmospheric dynamics around the mid-latitudes based on the quasi-geostrophic
 136 approximation, and simulates a jet-like zonal flow when suitable values for the param-
 137 eters are chosen. A vertical structure of two discrete layers, which we assume to have
 138 equal depth, is the minimal vertical resolution that allows the representation of baro-
 139 clinic processes (Holton, 2004).

Subgrid-scale eddies and bottom friction are modeled by biharmonic viscosity, while
 in the upper layer (i.e. $i = 1$) large-scale forcing is provided by a prescribed background-
 flow $U = 0.6$ as, for instance, in Cotter et al. (2018); Jansen and Held (2014). The ex-
 ternal forcing leads to the formation of a jet stream with non-trivial meridional struc-
 ture whose location experiences meridional shifts - a prominent feature of the observed
 atmospheric jet stream (Feldstein, 1998; James & Dodd, 1996; Riehl, Yeh, & La seur,
 1950). Since we consider a non-dimensional description, the horizontal extensions have
 been rescaled to a $2\pi \times 2\pi$ square. Finally the evolution equations for the potential vor-
 ticities (PVs)

$$q_i(\mathbf{x}, t) = \nabla^2 \psi_i + (-1)^i \frac{k_d^2}{2} (\psi_1 - \psi_2) + \beta y \quad i \in \{1, 2\}$$

on the horizontal plane $\mathbf{x} = (x \ y)^T \in \mathbb{R}^2$, where x and y denote the zonal and the merid-
 ional directions respectively, read

$$\frac{\partial q_1}{\partial t} = -J(\psi_1 - Uy, q_1) - \nabla^2(\nu_1 \nabla^4 \psi_1) \quad , \quad (1a)$$

$$\frac{\partial q_2}{\partial t} = -J(\psi_2, q_2) - \nabla^2(\nu_2 \nabla^4 \psi_2) - \tau_f^{-1} \nabla^2 \psi_2 \quad , \quad (1b)$$

where $\psi_i(\mathbf{x}, t)$ $i \in \{1, 2\}$ are the corresponding streamfunctions and $\tau_f = 10$ the fric-
 tional time-scale. The term $k_d^2/2 = (2f_0/Nh)^2$ quantifies the strength of the shear be-
 tween the two layers and, hence, also the intensity of the baroclinic instability ($N = 1.2 \cdot$
 10^{-2} being the Brunt-Väisälä frequency, $h = 200$ the mean depth of the layers and $f \approx$
 $f_0 + \beta y$ the approximate Coriolis term with $f_0 = 1$ and $\beta = 0.509$). These values imply
 a Rossby deformation radius $k_d^{-1} \approx 0.85$. The strength of the effective damping of
 the subgrid-scale eddies is quantified by $\nu_i = \nu(\psi_i)$. We follow Jansen and Held (2014);
 Leith (1996) and set

$$\nu_i(\mathbf{x}) = C_{Leith} \Delta^6 |\nabla^4 \psi_i| \quad i \in \{1, 2\}$$

where $C_{Leith} = 0.005$ is an empirical constant and Δ is the size of the numerical grid-
 spacing. ∇ and ∇^2 denote, respectively, the horizontal gradient and the Laplacian op-

erator, while the Jacobian operator J is defined as

$$J(A, B) = \frac{\partial A}{\partial x} \frac{\partial B}{\partial y} - \frac{\partial A}{\partial y} \frac{\partial B}{\partial x} .$$

In order to have a better defined distinction between slow and fast modes, we rewrite equations (1) as barotropic and baroclinic modes by assuming that barotropic modes evolve more slowly than baroclinic modes. Barotropic and baroclinic streamfunctions, ψ_B and ψ_T , can be defined as:

$$\psi_B = \frac{1}{2}(\psi_1 + \psi_2) , \quad \psi_T = \frac{1}{2}(\psi_1 - \psi_2) ;$$

which lead to the corresponding barotropic and baroclinic potential vorticities, q_B and q_T ,

$$q_B = \nabla^2 \psi_B + \beta y , \quad q_T = \nabla^2 \psi_T - k_d^2 \psi_T . \quad (2)$$

It can easily be shown that barotropic and baroclinic PVs can also be written as

$$q_B = \frac{1}{2} (q_1 + q_2) , \quad q_T = \frac{1}{2} (q_1 - q_2) ,$$

and we can use these relations to determine the evolution equations for q_B and q_T from (1). After some manipulations we obtain

$$\begin{aligned} \frac{dq_B}{dt} = & -J(\psi_B - \frac{1}{2}Uy, q_B) - J(\psi_T - \frac{1}{2}Uy, q_T) - \frac{1}{2}\tau_f^{-1} (\nabla^2 \psi_B - \nabla^2 \psi_T) \\ & - \frac{C_{Leith}\Delta^6}{2} \nabla^2 (|\nabla^4(\psi_B + \psi_T)| \nabla^4(\psi_B + \psi_T) + |\nabla^4(\psi_B - \psi_T)| \nabla^4(\psi_B - \psi_T)) , \end{aligned} \quad (3a)$$

$$\begin{aligned} \frac{dq_T}{dt} = & -J(\psi_T - \frac{1}{2}Uy, q_B) - J(\psi_B - \frac{1}{2}Uy, q_T) + \frac{1}{2}\tau_f^{-1} (\nabla^2 \psi_B - \nabla^2 \psi_T) \\ & - \frac{C_{Leith}\Delta^6}{2} \nabla^2 (|\nabla^4(\psi_B + \psi_T)| \nabla^4(\psi_B + \psi_T) - |\nabla^4(\psi_B - \psi_T)| \nabla^4(\psi_B - \psi_T)) , \end{aligned} \quad (3b)$$

where the derivative operator d is only with respect to time, and the biharmonic viscosity coefficient has been decomposed in its constant and non-constant parts. The unforced inviscid part of system (3) is Hamiltonian with the Hamiltonian H given by

$$H(q_B, q_T) = \frac{1}{2} \iint [(\nabla \psi_B)^2 + (\nabla \psi_T)^2 + k_d^2 \psi_T^2] d\mathbf{x} , \quad (4)$$

corresponding to the total energy. The Hamiltonian allows for the following relationships, which we will use in the next Section,

$$\frac{\partial H}{\partial q_B} = -\psi_B , \quad \frac{\partial H}{\partial q_T} = -\psi_T .$$

140 For a general review of Hamiltonian mechanics and its application to geophysical fluid
141 dynamics see for example Badin and Crisciani (2018); Salmon (1988); Shepherd (1990).

142 The numerical truncation affects deeply the dynamics by introducing a larger er-
143 ror at coarser resolutions. In particular, since smaller scales are not represented, the re-
144 injection of kinetic energy from the unresolved into the resolved scales is reduced. This
145 implies that the kinetic energy is dependent on the grid resolution (Dwivedi et al., 2019;
146 Jansen & Held, 2014) leading, for instance, to a misrepresentation of the eddy kinetic
147 energy at coarser resolutions (Juricke et al., 2019; Porta Mana & Zanna, 2014). Since
148 the computational cost of high resolution simulations is often prohibitive, we aim at re-
149 covering the large scale variability induced by the faster modes, and hence increase the
150 eddy kinetic energy at lower resolutions, by correcting the numerical error through the
151 introduction of a stochastic parameterization for the sub-grid scales. In the next Sec-
152 tion we present a stochastic parametrization which ensures that the stochastic noise does
153 not break the inherent energy balance of the system.

3 Energy consistent stochastic parameterization

154
155
156
157
158
159
160
161
162
163
164
165
166
167
168
169
170
171
172
173

Our underlying model assumption is that there are many fast baroclinic modes which drive both the resolved and the large-scale barotropic modes, and which can be efficiently represented by a stochastic Ansatz. Since barotropic modes are mainly large-scale, its spectra are dominated by the large-scales, and the noise forcing can effectively affect just the baroclinic modes. Hence, as in Gugole and Franzke (2019), we represent the unresolved fast sub-grid processes by means of a stochastic forcing, which we assume to act directly on the baroclinic mode and only indirectly on the barotropic mode. In order to introduce only dynamically consistent perturbations, we employ the projection operator method proposed in Frank and Gottwald (2013) to construct a stochastic forcing such that the energy of the unforced inviscid core of the 2-layer QG model is preserved. This choice allows to retain the balance between the external forcing and the dissipation, while redistributing the energy among the scales. The approach by Frank and Gottwald (2013) also introduces seamlessly state-dependent noise and dissipation. This potentially also allows for a realistic representation of subgrid-scale effects as in previous studies (Berner, Shutts, Leutbecher, & Palmer, 2009; Dwivedi et al., 2019; Franzke et al., 2015; Jansen et al., 2015) since this approach also predicts the corresponding nonlinear damping. In previous approaches the damping needed to be tuned in order to ensure numerical stability (Whitaker & Sardeshmukh, 1998; Zhang & Held, 1999). Our approach avoids any empirical tuning of the damping.

Since Gaussian white noise exists only as a distribution, stochastic evolution equations should be interpreted as integral equations (Gardiner, 2009; Pavliotis & Stuart, 2008). Hence we slightly change notation towards this interpretation, where we dropped the integral symbol in order to have a not too heavy notation. In this work we adopt Itô's interpretation of the stochastic integrals (Gardiner, 2009). We propose the following stochastically forced modification of the 2-layer QG system (1)

$$dq_B = - \left(J(\psi_B - \frac{1}{2}Uy, q_B) + J(\psi_T - \frac{1}{2}Uy, q_T) \right) dt - \frac{1}{2}\tau_f^{-1} (\nabla^2\psi_B - \nabla^2\psi_T) dt - \frac{C_{Leith}\Delta^6}{2} \nabla^2 (|\nabla^4(\psi_B + \psi_T)| \nabla^4(\psi_B + \psi_T) + |\nabla^4(\psi_B - \psi_T)| \nabla^4(\psi_B - \psi_T)) dt, \quad (5a)$$

$$dq_T = - \left(J(\psi_T - \frac{1}{2}Uy, q_B) + J(\psi_B - \frac{1}{2}Uy, q_T) \right) dt + \frac{1}{2}\tau_f^{-1} (\nabla^2\psi_B - \nabla^2\psi_T) dt - \frac{C_{Leith}\Delta^6}{2} \nabla^2 (|\nabla^4(\psi_B + \psi_T)| \nabla^4(\psi_B + \psi_T) - |\nabla^4(\psi_B - \psi_T)| \nabla^4(\psi_B - \psi_T)) dt + \Sigma(\mathbf{x}, t) dW_t + dY_t, \quad (5b)$$

$$dY_t = Bdt + SdW_t, \quad (5c)$$

where W_t denotes a Wiener process. The auxiliary stochastic process Y_t , which is parametrized by $B = B(\mathbf{x}, t)$ and $S = S(\mathbf{x}, t)$, is determined to ensure that the stochastic forcing $\Sigma(\mathbf{x}, t)dW_t$ preserves the energy given by the Hamiltonian (4) (Frank & Gottwald, 2013). Using Itô's formula (Gardiner, 2009) the change in the energy is given by

$$\begin{aligned} dH &= \frac{\partial H}{\partial q_B} \cdot dq_B + \frac{\partial H}{\partial q_T} \cdot dq_T + \frac{1}{2} \frac{\partial^2 H}{\partial q_T \partial q_T} : dq_T dq_T^T \\ &= \mu_H dt + \sigma_H dW_t, \end{aligned}$$

where the matrix inner product is defined as $A : B = a_{ij}b_{ij} = Tr(AB^T)$, and where

$$\begin{aligned}
 \mu_H &= +\psi_B \cdot \left(J(\psi_B - \frac{1}{2}Uy, q_B) + J(\psi_T - \frac{1}{2}Uy, q_T) + \frac{1}{2}\tau_f^{-1} (\nabla^2\psi_B - \nabla^2\psi_T) \right) \\
 &+ \frac{C_{Leith}\Delta^6}{2} \psi_B \cdot \nabla^2 (|\nabla^4(\psi_B + \psi_T)| \nabla^4(\psi_B + \psi_T) + |\nabla^4(\psi_B - \psi_T)| \nabla^4(\psi_B - \psi_T)) dt \\
 &+ \psi_T \cdot \left(J(\psi_T - \frac{1}{2}Uy, q_B) + J(\psi_B - \frac{1}{2}Uy, q_T) - \frac{1}{2}\tau_f^{-1} (\nabla^2\psi_B - \nabla^2\psi_T) - B_t \right) \\
 &+ \frac{C_{Leith}\Delta^6}{2} \psi_T \cdot \nabla^2 (|\nabla^4(\psi_B + \psi_T)| \nabla^4(\psi_B + \psi_T) + |\nabla^4(\psi_B - \psi_T)| \nabla^4(\psi_B - \psi_T)) dt \\
 &+ \frac{1}{2} \frac{\partial^2 H}{\partial q_T \partial q_T} : (\Sigma + S_t)(\Sigma + S_t)^T, \\
 \sigma_H &= -\psi_T \cdot (\Sigma + S_t) \\
 &= \nabla_{q_T} H \cdot (\Sigma + S_t).
 \end{aligned}$$

Our aim is to control the stochastic forcing in order to preserve the energetic balance between the external forcing and the dissipation. In order to guarantee the total energy not to be affected by the stochastic forcing, we set σ_H and the sum of those terms in μ_H due to the stochastic processes to be zero. The auxiliary process must be constructed to force the deviations from the manifold of constant energy, caused by the stochastic forcing $\Sigma(\mathbf{x}, t)dW_t$, back onto the manifold. It should therefore only have components orthogonal to the manifold of constant energy. Thus we define a projection operator \mathbb{P} , which projects onto the tangent space of the energy manifold, and we require $\mathbb{P}S = \mathbb{P}B = 0$. Since the Wiener process affects only the evolution equation of the baroclinic mode, it is sufficient to project onto the manifold of constant baroclinic energy, and we define the projection operator \mathbb{P} as

$$\begin{aligned}
 \mathbb{P} &= \mathbf{I} - \frac{1}{|\nabla_{q_T} H|^2} \nabla_{q_T} H (\nabla_{q_T} H)^T \\
 &= \mathbf{I} - \frac{1}{|\psi_T|^2} \psi_T \psi_T^T,
 \end{aligned}$$

where \mathbf{I} stands for the identity operator. Using $\mathbb{P}(\nabla_{q_T} H) = 0$, the condition $\sigma_H = 0$ provides an expression for S , while it is possible to determine B by considering only the terms of μ_H due to the introduction of the stochastic processes:

$$\begin{aligned}
 S &= -(\mathbf{I} - \mathbb{P})\Sigma, \\
 B &= +\frac{1}{2|\psi_T|^2} \left(\frac{\partial^2 H}{\partial q_T \partial q_T} : \mathbb{P}\Sigma\Sigma^T\mathbb{P} \right) \psi_T.
 \end{aligned}$$

We can now finally express our stochastic forced and damped 2-layer QG model (5) as

$$\begin{aligned}
 dq_B &= - \left(J(\psi_B - \frac{1}{2}Uy, q_B) + J(\psi_T - \frac{1}{2}Uy, q_T) \right) dt - \frac{1}{2}\tau_f^{-1} (\nabla^2\psi_B - \nabla^2\psi_T) dt \\
 &- \frac{C_{Leith}\Delta^6}{2} \nabla^2 (|\nabla^4(\psi_B + \psi_T)| \nabla^4(\psi_B + \psi_T) + |\nabla^4(\psi_B - \psi_T)| \nabla^4(\psi_B - \psi_T)) dt,
 \end{aligned} \tag{6a}$$

$$\begin{aligned}
 dq_T &= - \left(J(\psi_T - \frac{1}{2}Uy, q_B) + J(\psi_B - \frac{1}{2}Uy, q_T) \right) dt + \frac{1}{2}\tau_f^{-1} (\nabla^2\psi_B - \nabla^2\psi_T) dt \\
 &- \frac{C_{Leith}\Delta^6}{2} \nabla^2 (|\nabla^4(\psi_B + \psi_T)| \nabla^4(\psi_B + \psi_T) - |\nabla^4(\psi_B - \psi_T)| \nabla^4(\psi_B - \psi_T)) dt \\
 &+ \mathbb{P}\Sigma dW_t + \frac{1}{2|\psi_T|^2} \left(\frac{\partial^2 H}{\partial q_T \partial q_T} : \mathbb{P}\Sigma\Sigma^T\mathbb{P} \right) \psi_T dt.
 \end{aligned} \tag{6b}$$

174 The stochastic forced and damped 2-layer QG model (6) contains multiplicative noise
 175 and nonlinear damping, due to the specific definition of the projection operator. The mul-
 176 tiplicative noise is in fact a correlated additive multiplicative (CAM) noise (Majda, Franzke,

177 & Crommelin, 2009; Sardeshmukh & Sura, 2009). The interested reader may find more
 178 details about the necessary steps for the derivation of (6) in Frank and Gottwald (2013);
 179 Gugole and Franzke (2019).

180 In equations (6) the noise strength $\Sigma(\mathbf{x}, t)$, which specifies the spatial covariance
 181 of the noise, is still unspecified. In Gugole and Franzke (2019), it was shown that the
 182 choice of a dynamically consistent spatial structure of the noise covariance is crucial for
 183 a stochastic parametrization to be reliable. We propose in the next Section ways to pre-
 184 scribe the spatial structure.

185 4 The spatial covariance structure of the noise

We prescribe the spatial covariance of the noise by expressing $\Sigma(\mathbf{x}, t)$ through p dy-
 namically relevant patterns of the large-scale dynamics $\phi_i(\mathbf{x}, t)$, $i = 1, \dots, p$. In par-
 ticular, we write

$$\Sigma(\mathbf{x}, t) = \sum_{i=1}^p \gamma_i \phi_i(\mathbf{x}, t) \quad (7)$$

186 where the $\gamma_i \in \mathbb{R}$ are weights associated with each pattern.

187 We shall discuss here two choices of patterns ϕ_i : first, Empirical Orthogonal Func-
 188 tions (EOFs), which capture time-invariant climatological patterns, and, second, pat-
 189 terns obtained by means of Dynamical Mode Decomposition (DMD), which describe time-
 190 varying, dynamically adapted dominant patterns.

191 4.1 Empirical Orthogonal Functions

192 4.1.1 Theory

EOF is a multivariate statistical analysis technique that derives the dominant pat-
 terns of variability from a n -dimensional field, usually indexed by location in space (von
 Storch, 1995; von Storch & Zwiers, 2003). Let \mathbf{X} be an n -dimensional random vector,
 whose mean is assumed to be zero; otherwise the anomalies of the field with respect to
 the mean should be considered. At its first stage the EOF analysis computes the vec-
 tor ϕ_1 with $\|\phi_1\| = 1$ such that

$$\epsilon_1 = \mathbb{E} \left(\|\mathbf{X} - \langle \mathbf{X}, \phi_1 \rangle \phi_1\|^2 \right) \quad (8)$$

is minimized, where we denoted with \mathbb{E} the expectation operator, the vector norm by
 $\|\cdot\|$ and the inner product with $\langle \cdot, \cdot \rangle$. Equation (8) describes the projection of the field
 \mathbf{X} onto a 1-dimensional subspace spanned by the vector ϕ_1 . Minimizing ϵ_1 is equivalent
 to maximizing the variance of \mathbf{X} contained in this subspace, in fact it can be shown that

$$\epsilon_1 = \text{Var}(\mathbf{X}) - \text{Var}(\langle \mathbf{X}, \phi_1 \rangle),$$

193 where the variance of \mathbf{X} is defined to be the sum of the variances of its elements. Let
 194 Γ denote the covariance matrix of \mathbf{X} . It can be shown that ϕ_1 is an eigenvector of Γ with
 195 corresponding eigenvalue λ_1 . Therefore, the minimum of equation (8) is achieved by the
 196 vector associated to the largest eigenvalue of Γ , i.e. vector ϕ_1 .

The same procedure is repeated to find the second EOF, which is the vector ϕ_2 with
 $\|\phi_2\| = 1$ minimizing

$$\epsilon_2 = \mathbb{E} \left(\left\| (\mathbf{X} - \langle \mathbf{X}, \phi_1 \rangle \phi_1) - \langle \mathbf{X}, \phi_2 \rangle \phi_2 \right\|^2 \right),$$

197 and corresponding to the second largest eigenvalue λ_2 of Γ . Finally we remark that Γ
 198 is an Hermitian matrix, hence its eigenvectors are orthogonal to one another. Moreover
 199 in case of translationally invariant systems they correspond to Fourier modes.

200

4.1.2 Constructing Σ using EOF

EOFs are computed on a time series of the baroclinic streamfunction (after the dynamics settled on the attractor) of the deterministic system (3) over a spatial grid with 128×128 elements. To construct the spatial structure of the noise, we compute a linear combination of the first p EOF patterns ϕ_i^{EOF} for $i = 1, \dots, p$ with weights given by the square roots of their corresponding eigenvalues λ_i^{EOF} $i = 1, \dots, p$ writing (7) as

$$\Sigma(\mathbf{x}) = \sum_{i=1}^p \sqrt{\lambda_i^{EOF}} \phi_i^{EOF}(\mathbf{x}). \quad (9)$$

201

202

Hence, Σ is constant in time and $\Lambda = \Sigma \Sigma^T$ corresponds to the variance of the QG model's baroclinic stream function as approximated by the first p EOFs.

203

204

205

206

207

208

209

210

211

EOF patterns As in the majority of cases, the spectrum of the EOF eigenvalues rapidly decay, and the first 5 EOFs carry circa 95% of the variance. Higher EOFs do not carry significant variance and hence might be considered as numerical noise (see Figure 1a). EOFs 1-2 (Figures 1b-1c) represent the predominant traveling Rossby wave supported by the 2-layer QG model. EOF 3 (Figure 1d) does not represent any wave but captures the spatial dominant pattern associated with the jet stream. EOFs 4-5 (Figures 1e-1f) capture again dominant wave patterns. In our numerical simulations, we use either only the first two EOFs, corresponding to $\Lambda \approx 0.36$, or the first five EOFs, i.e. $\Lambda \approx 0.47$.

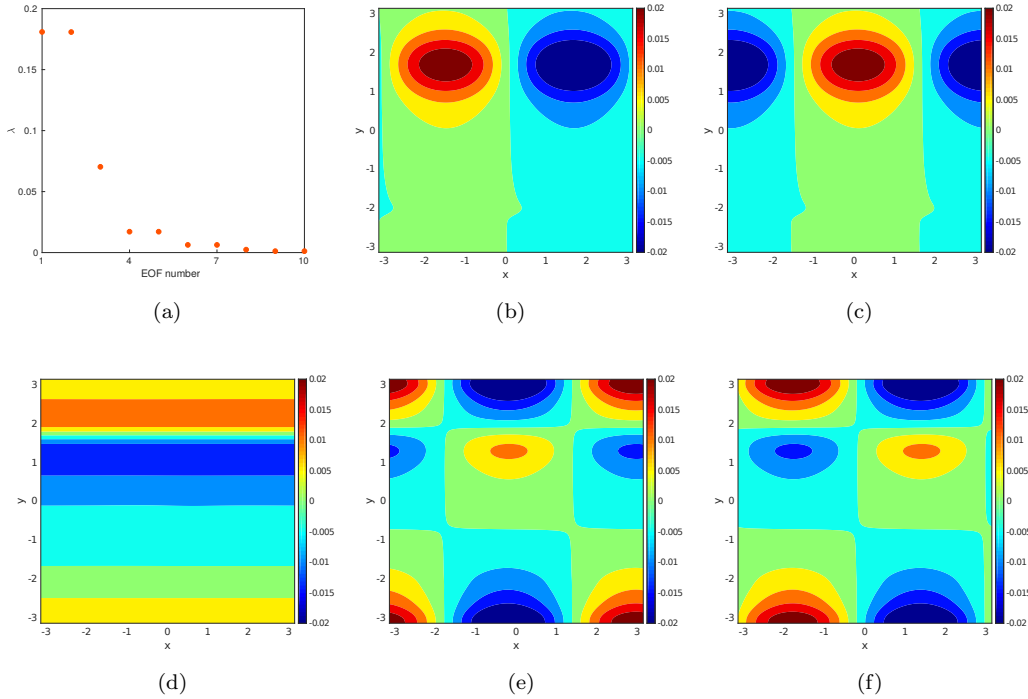


Figure 1. EOF singular values spectrum of the first 10 eigenvectors and first 5 EOF patterns. From left to right: top row; eigenvalues spectrum, EOF-1 and EOF-2; bottom row; EOF-3, EOF-4 and EOF-5.

212

213

EOFs are widely used in the climate science, thanks to their robust computability given a large available data set. Nonetheless EOFs have known limitations. In par-

214 particular, their physical interpretation is restricted. While it is possible to associate the
 215 first EOF with observed physical features, this becomes increasingly complicated for higher-
 216 order EOFs, because of the orthogonality constraint (von Storch & Zwiers, 2003). We
 217 therefore introduce in the next Section DMDs, which capture relevant modes, adapted
 218 to the prevailing dynamics.

219 4.2 Dynamic Mode Decomposition

220 4.2.1 DMD and the Koopman operator

221 Here we briefly present the Koopman operator and its connection with Dynamic
 222 Mode Decomposition (DMD). Detailed reviews about the Koopman operator can be found,
 223 for instance, in (Budišić, Mohr, & Mezić, 2012; Mezić, 2013), while theory and applica-
 224 tions of DMD are provided, among others, in (Kutz et al., 2016; Schmid, 2010; Tu et al.,
 225 2014).

Let $\dot{x} = f(x)$ denote a general continuous-time dynamical system with initial con-
 dition $x(0) = x_0 \in \mathbb{R}^n$. On the assumption that there exists a unique solution of this
 initial value problem, it is possible to introduce the flow map φ_t such that $x(t) = \varphi_t(x_0)$.
 Define an arbitrary observable $\psi(x)$. The value of this observable ψ , which the system
 sees starting in x_0 at time t , is

$$\psi(t, x_0) = \psi(\varphi_t(x_0)) .$$

The Koopman operator is a semigroup of operators \mathcal{K}_t , acting on the space of observ-
 ables parameterized by time t

$$\mathcal{K}_t \psi(x_0) = \psi(\varphi_t(x_0)) .$$

It is important to underline that the operator \mathcal{K}_t is linear also in case of non-linear dy-
 namics f , thus it makes sense to consider its spectral properties, but the eigenfunctions
 of the Koopman operator are not necessarily linear. Dynamic mode decomposition is a
 data-driven technique for computing an approximation of the Koopman modes. Con-
 sider a dynamical system as above, and two sets of data, either of the state variables or
 of any observable of them,

$$\mathbf{X} = \begin{pmatrix} | & | & \cdots & | \\ \mathbf{x}_1 & \mathbf{x}_2 & \cdots & \mathbf{x}_m \\ | & | & \cdots & | \end{pmatrix} \quad \mathbf{X}' = \begin{pmatrix} | & | & \cdots & | \\ \mathbf{x}'_1 & \mathbf{x}'_2 & \cdots & \mathbf{x}'_m \\ | & | & \cdots & | \end{pmatrix}$$

such that

$$\begin{aligned} \mathbf{x}_k &= \mathbf{x}(t_k) \in \mathbb{R}^n , & \mathbf{x}'_k &= \mathbf{x}(t_k + \delta t) = \mathcal{K}_{\delta t} \mathbf{x}_k , \\ \mathbf{x}_k &= \mathbf{x}(t_{k-1} + \Delta t) = \mathcal{K}_{\Delta t} \mathbf{x}_{k-1} , & \mathbf{x}'_k &= \mathbf{x}(t_{k-1} + \delta t + \Delta t) = \mathcal{K}_{\Delta t} \mathbf{x}'_{k-1} , \end{aligned}$$

226 where $m\Delta t$ defines the time window, and $\delta t \leq \Delta t$ determines the accuracy of the re-
 227 constructed dynamics. It is important to mention that matrices \mathbf{X} and \mathbf{X}' are assumed
 228 to be *tall and skinny*, i.e. it is assumed that the size n of a snapshot is larger than the
 229 number $m-1$ of snapshots. In the DMD algorithm the Koopman operator is approx-
 230 imated by means of a least square fit operator $\mathbf{K}_{\delta t}$ relating data $\mathbf{X}' \approx \mathbf{K}_{\delta t} \mathbf{X}$. The nu-
 231 merically stable algorithm, based on a singular value decomposition and outlined for the
 232 first time in Schmid (2010) and improved in Tu et al. (2014), allows for a low-rank $r \leq$
 233 m representation of the operator $\mathbf{K}_{\delta t}$ onto the first r EOF modes of matrix \mathbf{X} . Details
 234 about the algorithm, as well as a MATLAB[®] function, are provided in Kutz et al. (2016).
 235 The DMD modes ϕ_i are the (complex) eigenvectors of $\mathbf{K}_{\delta t}$, and they are not orthogo-
 236 nal. Furthermore, they represent dynamically relevant structures, the so called Koop-
 237 man modes, whose temporal oscillation periods and their growth rates are provided by
 238 their associated (complex) eigenvalues λ_i . There exists a real eigenvalue $\lambda_0 = 1$ with

239 eigenvector ϕ_0 corresponding to the mean of the observable \mathbf{x} . Whereas EOF decomposes
 240 the dynamics according to dominant stationary patterns, DMD decomposes the dynam-
 241 ics according to its local in time oscillatory behavior.

242 We remark that there exists an intimate relationship between the DMD matrix $\mathbf{K}_{\delta t}$
 243 and the Koopman operator, first realized in Rowley et al. (2009). However, it is well es-
 244 tablished that DMD provides a good approximation of the actual Koopman operator -
 245 and hence constitutes a good representation of the underlying dynamics - only in case
 246 of sufficiently rich and diverse observations (Budišić et al., 2012; Tu et al., 2014; Williams
 247 et al., 2015). The least square approximation of the Koopman operator suggests that
 248 a good approximation is guaranteed for sufficiently small δt and for sufficiently small time
 249 intervals $m\Delta t$ such that the dynamics is essentially linear.

250 4.2.2 Defining the noise covariance by means of DMD

251 As for EOFs, we choose the baroclinic stream function ψ_T to determine the DMD
 252 modes. In deterministic systems the eigenvalues of the Koopman operator lie on the com-
 253 plex unit circle and, apart from the eigenvalue λ_0^{DMD} corresponding to the mean mode,
 254 appear as complex conjugate pairs. In stochastic systems, however, eigenvalues inside
 255 or outside the unit circle may appear; see Figure 2 for an instance of the DMD eigen-
 256 values for the stochastic QG model (6). Since we want to capture the dynamically rel-
 257 evant patterns of the deterministic QG system, we exclude all eigenmodes ϕ_i^{DMD} whose
 258 eigenvalues do not lie on the unit circle (within some tolerance to account for numeri-
 259 cal noise). The eigenvectors and eigenvalues are sorted with decreasing real part accord-
 260 ing to $\lambda_0^{DMD} = 1 > \text{Re}(\lambda_1^{DMD}) \geq \dots \geq \text{Re}(\lambda_r^{DMD})$. For each pair $(\lambda_i^{DMD}, \phi_i^{DMD})$
 261 we choose also its complex conjugate pair. To give a graphical illustration, the blue dot
 262 in Figure 2 corresponds to λ_0^{DMD} , while the green and orange dots to λ_1^{DMD} and λ_2^{DMD} ,
 263 respectively, and their complex conjugates. The eigenmodes corresponding to the eigen-
 264 values marked in red in Figure 2 are neglected since they are away from the unit circle.

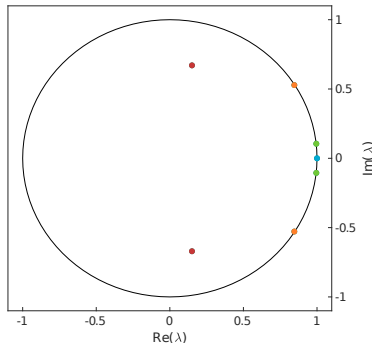


Figure 2. Example of DMD eigenvalues spectrum with parameters $m = 16$, $r = 7$, $\delta t = 0.1$, $\Delta t = 3\delta t$. The blue dot corresponds to λ_0^{DMD} , while the green, orange and red ones to λ_1^{DMD} , λ_2^{DMD} and λ_3^{DMD} , respectively, and their complex conjugates.

To construct the spatial structure $\Sigma(\mathbf{x}, t)$ of the noise, we choose the first $p = 2$ dominant DMD patterns $\phi_{1,2}^{DMD}$ obtained from the low-resolution simulation of the stochastic 2-layer QG system (6). Since the eigenvalues and the eigenfunctions are now com-

plex, each mode is considered together with its complex conjugate, hence Σ reads

$$\begin{aligned}\Sigma(\mathbf{x}, t) &= \frac{1}{2} \sum_{i=1}^2 ((\text{Re}(\lambda_i^{DMD}(t)) + i\text{Im}(\lambda_i^{DMD}(t))) (\text{Re}(\phi_i^{DMD}(\mathbf{x}, t)) + i\text{Im}(\phi_i^{DMD}(\mathbf{x}, t))) + \text{c.c.}) \\ &= \sum_{i=1}^2 (\text{Re}(\lambda_i^{DMD}(t)) \text{Re}(\phi_i^{DMD}(\mathbf{x}, t)) - \text{Im}(\lambda_i^{DMD}(t)) \text{Im}(\phi_i^{DMD}(\mathbf{x}, t))) , \quad (10)\end{aligned}$$

where $i^2 = -1$ and *c.c.* denotes the complex conjugate. Finally we normalize $\Lambda = \Sigma\Sigma^T$ to be either $\Lambda = \lambda_1^{EOF} + \lambda_2^{EOF} \approx 0.36$ or $\Lambda = \sum_{i=1}^5 \lambda_i^{EOF} \approx 0.47$. This is done to ensure that the noise has equal intensity both with EOFs and DMDs, and therefore have a fairer comparison of the results. To numerically estimate the first two complex conjugate DMD eigenpairs $(\lambda_i^{DMD}, \phi_i^{DMD})$ for $i = 1, 2$, we choose a small time interval $\delta t = 0.1$ (recall that δt needs to be chosen sufficiently small to allow for a reliable estimation of the DMD matrix $\mathbf{K}_{\delta t}$ which encodes the dynamics). Furthermore we choose a time window of $m\Delta t = 4.8$ time units, which corresponds to roughly half an eddy turnover time for the parameters of our set-up (see Section 5.1 for details), and a separation of snapshots of $\Delta t = 3\delta t$ (implying $m = 16$). When numerically estimating singular value decompositions, only the first few singular vectors are reliable. An optimal truncation criterion was provided in Gavish and Donoho (2014) which, applied to our data, amounts to setting a low-rank approximation with $r = 7$ eigenmodes. We have tested that for the selected values of the parameters, DMD provides a good reconstruction of the dynamics in a time window of length $m\Delta t$ time units, as can be seen in Figure 3, where the actual dynamic is shown alongside the DMD reconstruction. Other sets of parameters corresponding to different time windows spanning between 2 and 10 time units have been tested, but this particular choice was the only one among those tested which does not present two eigenvalues with null imaginary part and real part very close to 1. This second mean-mode cannot be excluded by our procedure since the module of its corresponding eigenvalue is still very close to 1, but by plotting and comparing it to the other modes it can be seen that it is numerically spurious and not dynamically meaningful. We tested also the case with $m = 48$, $r = 7$, $\Delta t \equiv \delta t = 0.1$, i.e. we considered a time window of the same length and instead of sub-sampling - i.e. sampling consecutive snapshots in the same dataset every $\Delta t > \delta t$ - we chose a small value of r , but the results show that sub-sampling is more efficient in filtering out the numerical noise.

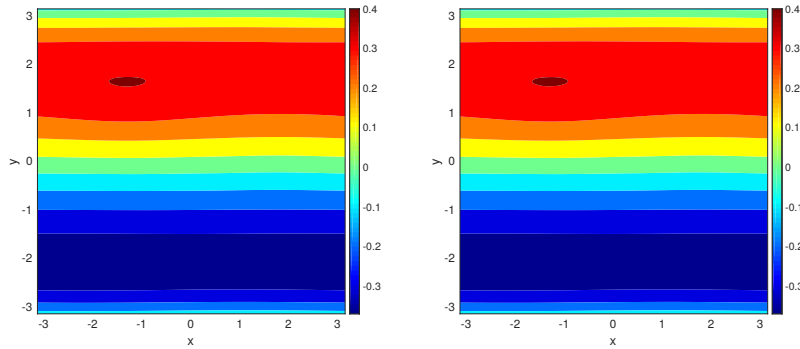


Figure 3. Comparison between the DMD reconstruction (left), and the true dynamics of ψ_T (right). Parameters of the DMD analysis were $m = 16$, $r = 7$, $\Delta t = 3\delta t$, $\delta t = 0.1$.

Contrary to EOFs, which require a long off-line simulation to be determined, the DMD pairs $\phi_{1,2}^{DMD}$ and $\lambda_{1,2}^{DMD}$ are computed on the fly after each $m\Delta t$ time units, hence

293 in this case Σ is a function also of time. Since for the first $m\Delta t$ time units the DMDs
 294 are not available yet, Σ is initialized using the first two EOFs. For simplicity we do not
 295 propagate the DMD modes by means of the Koopman operator, but keep them constant
 296 for $m\Delta t$ time units. We have checked that our results do not change much when prop-
 297 agating the DMDs in time to evaluate Σ at each time step. In our setup the DMD modes
 298 do not move much away from the initial state in the selected $m\Delta t$ time window, and this
 299 might be a reason why we obtained similar outcomes. For more complex models, a com-
 300 putationally cheaper alternative might be to recompute the DMD modes less often and
 301 to propagate the DMD modes for longer times.

302 *DMD patterns* In Figure 4 we show real and imaginary parts of the first two DMD
 303 modes as computed with the aforementioned set of parameters. The mode representing
 304 the mean has been neglected and only one of the two modes corresponding to a complex
 305 conjugate pair of eigenvalues is displayed. Since the DMD analysis is repeated along the
 306 simulation, the resulting modes are not exactly the same for the entire run, but the ed-
 307 dies move in the zonal direction. Moreover the eddies in the first mode slowly shift to-
 308 wards higher latitudes because of the meridional jet movement (as detected by the third
 309 EOF eigenvector). Since DMD decomposes the dynamics according to its oscillatory be-
 310 havior, the jet cannot be represented by a DMD eigenmode for the reason that it is not
 311 a wave. Hence in the DMD decomposition of the dynamics, the jet can be noticed only
 312 indirectly via its effect on the other modes. This is particularly evident when looking at
 313 the first mode as computed at the beginning (Figures 4a-4d) and at the end (Figures 4b-
 314 4e) of a simulation, when the difference in the meridional coordinate of the eddies is at
 315 its maximum. In this specific case only the first mode is affected by the jet, while the
 316 eddies in the other modes retain the same meridional coordinate while revolving in the
 317 zonal direction. Hence, for sake of simplicity, we display the second mode only as at the
 318 onset of a simulation (Figures 4c-4f).

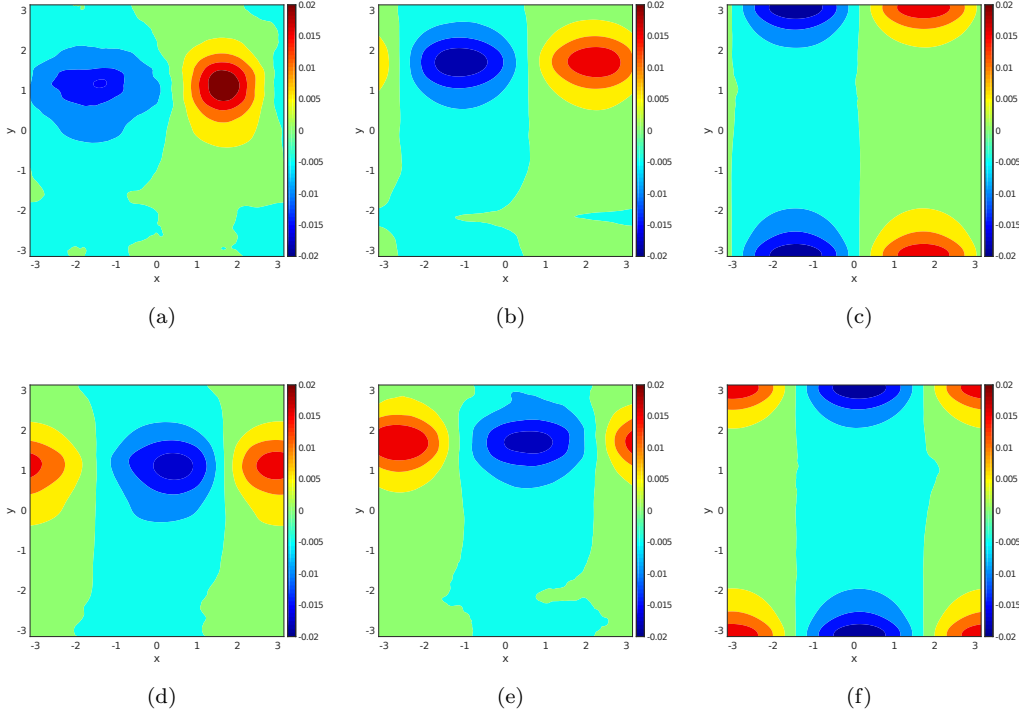


Figure 4. Real (top) and imaginary (bottom) parts of the first DMD mode at the beginning (left) and at the end (middle) of the simulation for $m = 16$, $r = 7$, $\Delta t = 3\delta t$, $\delta t = 0.1$. It can be noticed that in the course of the simulation, the eddies move in the zonal direction and shift towards high latitudes. This movement on the meridional axis is how DMD detects the jet. Real and imaginary parts of the second DMD mode (right) are also displayed. Differently from the eddies of the first mode, here they move only in zonal direction.

319 Real and imaginary parts of DMD mode number 1 resemble closely EOFs 1-2, al-
 320 though in the DMD mode the eddy patterns look smaller and less regular. Furthermore
 321 the eddies are centered in different meridional coordinates. This is likely due to the fact
 322 that EOFs capture directly the jet behavior, which is represented by EOF 3. EOFs 4-
 323 5 are the most comparable eigenvectors to the second DMD mode (Figure 4c-4f), but
 324 significant differences can be spotted for $y \in [0.8, 1.8]$, where some eddy structure is
 325 present in the EOF vectors but is absent in the DMD mode. This could be an artifact
 326 due to the orthogonality constraint of the EOF algorithm.

327 5 Results

328 We now present numerical results comparing outputs of a high-resolution simulation
 329 of the deterministic forced and damped 2-layer QG model (3) with those of a de-
 330 terministic low-resolution simulation as well as with the energy-consistent stochastic parametriza-
 331 tion (6) run at a low-resolution. Particular emphasis is given on comparing the effect of
 332 the respective prescribed spatial noise structures, using either (9) or (10) for EOFs and
 333 DMDs, respectively.

334

5.1 Model setup

335

336

337

338

339

340

341

342

343

344

As in most current ocean and climate models, we discretize equations (3)-(6) by means of finite differences in a grid-point based framework. The numerical discretization of the Jacobian operator in our QG model is based on the energy and enstrophy conserving scheme by Arakawa (1966). This scheme ensures that energy and enstrophy are conserved for all truncations in the inviscid case. In particular, this scheme does not require any numerical diffusion nor dissipation for numerical stability. For the time stepping of the deterministic part we employ a 4th order explicit Runge-Kutta method, while we use the Euler-Maruyama scheme for the stochastic terms (Pavliotis & Stuart, 2008). The inversion of the Laplacian is achieved in spectral space using Fast Fourier Transforms.

345

346

347

348

349

350

351

352

353

354

355

356

The simulations of the stochastic system (6) are run with a spatial resolution of 128×128 grid points and a time step of $dt = 10^{-3}$. All simulations start from the same initial condition, which we have assured to lie on the attractor by having employed a preceding integration of the deterministic equations at resolution 128×128 for 8000 time units. For each setting of the stochastic system we run the analyses on an ensemble of 10 independent simulations, and compare the outcomes with those of an equivalent deterministic low resolution and with those of a deterministic high resolution simulation. The latter, which will be referred also as reference solution, has been obtained by running the deterministic model (3) on a finer grid of 512×512 grid points. For numerical stability reasons, the reference solution is run with $dt = 10^{-4}$, and its results are projected on the coarser 128×128 spatial grid, to allow for a direct comparison with the outcomes of the respective low-resolution simulations.

357

5.2 Total energy

358

359

360

361

362

363

364

365

366

367

368

369

Looking at the total energy graphs of the different realizations in the various setups with EOF (orange) and DMD (green) reported in Figure 5, it can be noticed that on average the energy is stable with both techniques, fluctuating by about 1-2% of its absolute value; which is about the same as in a inviscid setting (Gugole & Franzke, 2019). Although the EOF ensemble members show more variance, when only the first two EOFs are used, the system seems to be slightly dissipative in time. This is particularly evident when looking at the ensemble mean (blue line in Figure 5a). The inclusion of EOFs 3-4-5 reduces the dissipative effect, but realizations with a clear increasing trend can be present (Figure 5c). Furthermore, some ensemble members drift away from the high resolution simulation. This also raises questions about long-term stability of the simulations, which we cannot currently resolve because of a too great computational expense of carrying out the simulations for much longer time periods.

370

371

372

373

374

375

376

377

On the other hand, the spread of the DMD ensemble members has less variance but well encloses the energy graph of the reference solution. Individual runs are more energetically stable, stay close to the reference solution, and the system seems to be less dissipative compared with the EOF based simulations (Figures 5b-5d). This suggests that the usage of a dynamically adapted noise structure may help the numerical model to remain on the manifold of constant energy and in a dynamically consistent flow regime. In any case deviations from the mean are less than 2%. Hence they might be considered as negligible.

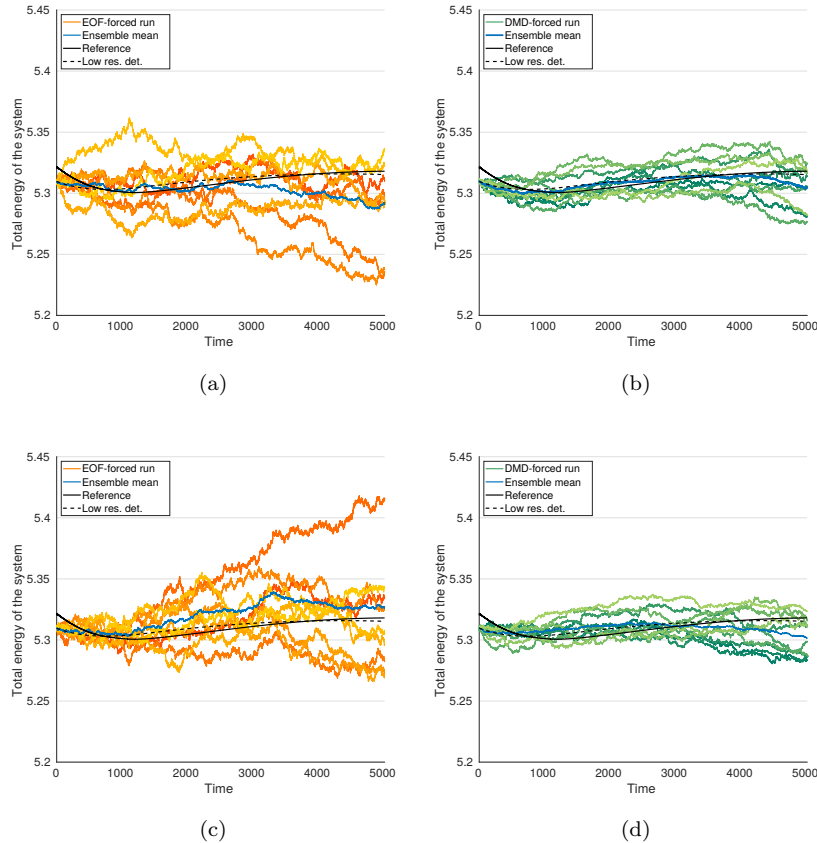


Figure 5. Total energy graphs for stochastic simulations using EOFs (left) or DMDs (right). The case $\Lambda \approx 0.36$, corresponding to the first two EOFs, is displayed in the top row, while the scenario $\Lambda \approx 0.47$ (first five EOFs) is shown in the bottom row. The parameters for DMD have been set as follows: $p = 2$, $m = 16$, $r = 7$, $\delta t = 0.1$, $\Delta t = 3\delta t$. Each stochastic ensemble contains 10 realizations.

378

5.3 Eddy kinetic energy

In order to compute the eddy kinetic energy (EKE), we first computed the horizontal velocities for the barotropic and baroclinic modes from the respective streamfunctions using

$$u = -\frac{\partial\psi}{\partial y}, \quad v = \frac{\partial\psi}{\partial x},$$

379

380

381

382

383

384

385

386

where u is the zonal and v the meridional velocity. Then we considered a time window of k time units to compute the temporal mean velocities, i.e. \bar{u}_B , \bar{v}_B and \bar{u}_T , \bar{v}_T for barotropic and baroclinic modes respectively. Afterwards for each time unit we computed the deviations from the mean, e.g. $u'_B(t) = u_B(t) - \bar{u}_B$, and used these quantities to compute the EKE for each grid point for all t . As a last step we averaged in time and then also in the zonal direction, therefore the EKE is displayed simply as a function of the meridional direction y (Figures 6-7); or we averaged only in the zonal direction and looked at the time evolution of the EKE projected on the meridional coordinate (Figure 8).

387

388

389

Since the system does not have any annual cycle or similar, we split the time series in windows of 1000 time units, and consider each window individually. Such a length of the time intervals ensures one not to be looking just at transient dynamics while con-

390 sidering small movements of the jet, due to its low frequency variability. Although the
 391 time-averaged EKE shows a bi-modal behavior in all windows, the meridional location
 392 of the peaks varies according to the jet movement. Hence we want to check how well the
 393 stochastic parameterization keeps track of the jet shift. The time-averaged EKE of the
 394 baroclinic mode for $t \in [1000, 2000]$ and for $t \in [3000, 4000]$ in the different stochas-
 395 tic setups with EOF (orange) and DMD (green) are reported in Figures 6 and 7, respec-
 396 tively. The EKE of the barotropic mode shows similar results as for the baroclinic mode,
 397 hence, it is not reported here. Figure 8 show the time evolution of the barotropic EKE
 398 for $t \in [3000, 4000]$ in case of the low resolution deterministic run, one stochastic simu-
 399 lation with EOFs 1-2-3-4-5 and $\Lambda \approx 0.47$, one realization with DMDs and $\Lambda \approx 0.47$,
 400 and for the reference solution. Similar conclusions hold also for the time evolution of the
 401 baroclinic PV.

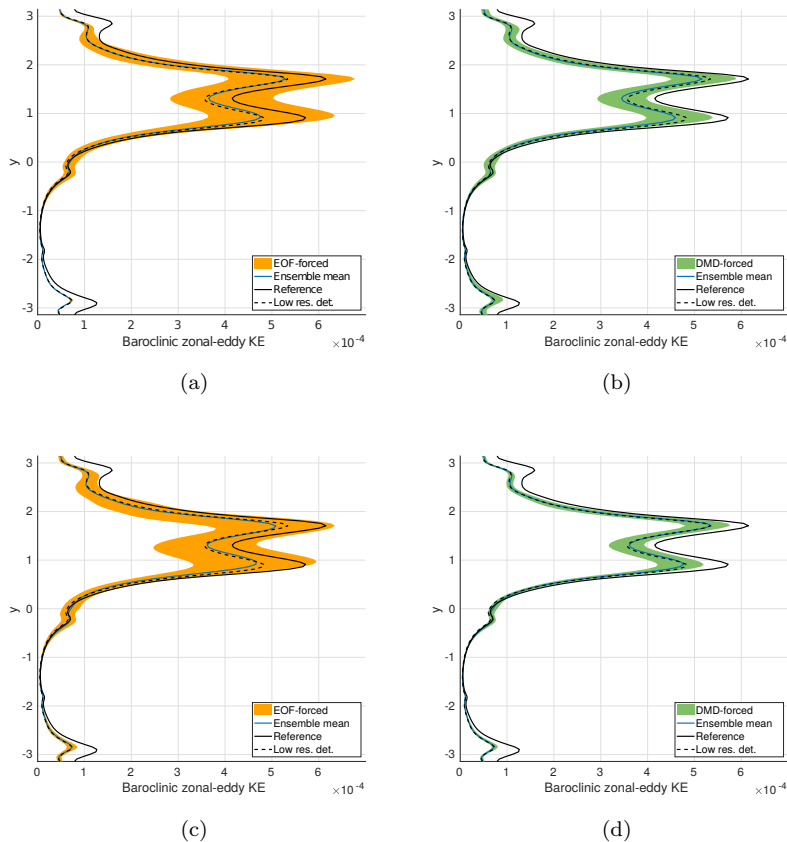


Figure 6. Baroclinic EKE for $t \in [1000, 2000]$ for stochastic simulations using EOFs (left) or DMDs (right). The case $\Lambda \approx 0.36$, corresponding to the first two EOFs, is displayed in the top row, while the scenario $\Lambda \approx 0.47$ (first five EOFs) is shown in the bottom row. The parameters for DMD have been set as follows: $p = 2$, $m = 16$, $r = 7$, $\delta t = 0.1$, $\Delta t = 3\delta t$. Each stochastic ensemble contains 10 realizations.

402 Both for $t \in [1000, 2000]$ and $t \in [3000, 4000]$ it can be seen that the ensemble
 403 forced by EOFs 1-2 has overshoots, which are compensated in the mean (blue line in Fig-
 404 ures 6 and 7) by simulations with lower EKE. This is particularly evident at later times
 405 (Figure 7), where the uncertainties grow in time and the single members do not display
 406 a coherent behavior, i.e. different realizations have different meridional locations for the

407 bi-modal structure and rather different EKE amplitudes. The introduction of EOFs 3-
 408 4-5 reduces the overshoots, but has also lower undershoots and does not help the ensam-
 409 ble members to maintain a coherent behavior for longer times. It can be further noticed
 410 in Figure 7 that, both with EOFs 1-2 and with EOFs 1-2-3-4-5, the EKE of the stochas-
 411 tic realizations is shifted to too high meridional positions. On the other hand the DMD
 412 forced ensembles have less variance and do not always enclose the reference solution, but
 413 they remain close to it and they follow quite well the meridional movement of the jet.
 414 Furthermore in the DMD ensembles, the uncertainties grow much more slowly in time,
 415 allowing the single members to display a coherent behavior also at later stages of the sys-
 416 tem evolution.

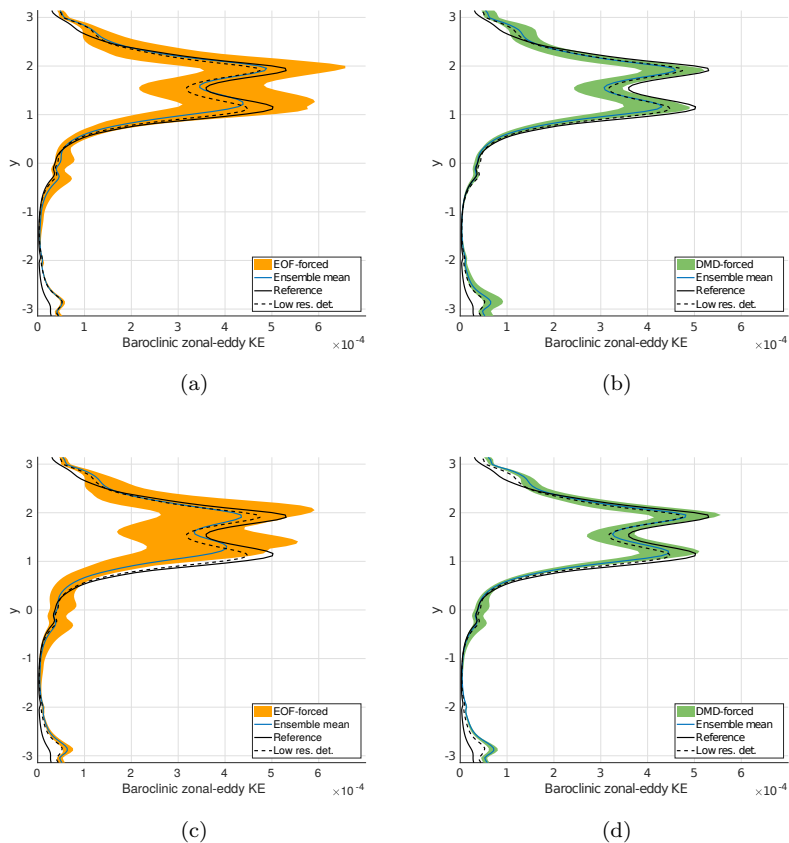


Figure 7. Baroclinic EKE for $t \in [3000, 4000]$ for stochastic simulations using EOFs (left) or DMDs (right). The case $\Lambda \approx 0.36$, corresponding to the first two EOFs, is displayed in the top row, while the scenario $\Lambda \approx 0.47$ (first five EOFs) is shown in the bottom row. The parameters for DMD have been set as follows: $p = 2$, $m = 16$, $r = 7$, $\delta t = 0.1$, $\Delta t = 3\delta t$. Each stochastic ensemble contains 10 realizations.

417 By looking at the time evolution of the barotropic EKE for $t \in [3000, 4000]$ (Fig-
 418 ure 8) we can notice that while the deterministic low resolution captures the main fea-
 419 tures, like the meridional shift of the positive EKE at $y \approx 1$, other characteristics are
 420 in general underestimated, for instance the amplitude of the eddy kinetic energy at $y \approx$
 421 -3 or at $y \approx 2$ for $t \in [3000, 3200]$, see Figures 8a and Figure 8d. Some of these prop-
 422 erties are indeed recovered by the DMD forced simulation, see for example the enforced
 423 EKE at $y \approx 2$ or at $y \approx -3$ in Figure 8c, while the EOFs induced stochastic forcing

424 does not recover them, and creates spurious EKE, see for instance at $y \approx 3$ for $t \in [3400, 3600]$
 425 in Figure 8b. Some spurious EKE at $y \approx 3$ can be noticed also in the DMD-forced simulation,
 426 but of smaller amplitude with respect to EOFs. Similar outcomes hold also in
 427 case of the baroclinic EKE, and are hence not reported here.

428 These results suggest that the use of a dynamically adapted noise covariance ma-
 429 trix in stochastic parameterizations might be better suited to model phenomena, which
 430 do not reach statistical equilibrium, while keeping track of the large scale dynamics. More-
 431 over, considering the wide usage of DMD to detect dynamical features like instabilities
 432 and bifurcations (Bagheri, 2013; Budišić et al., 2012; Kutz et al., 2016), a dynamically
 433 adapted spatial correlation might more easily foster the system towards tipping points.

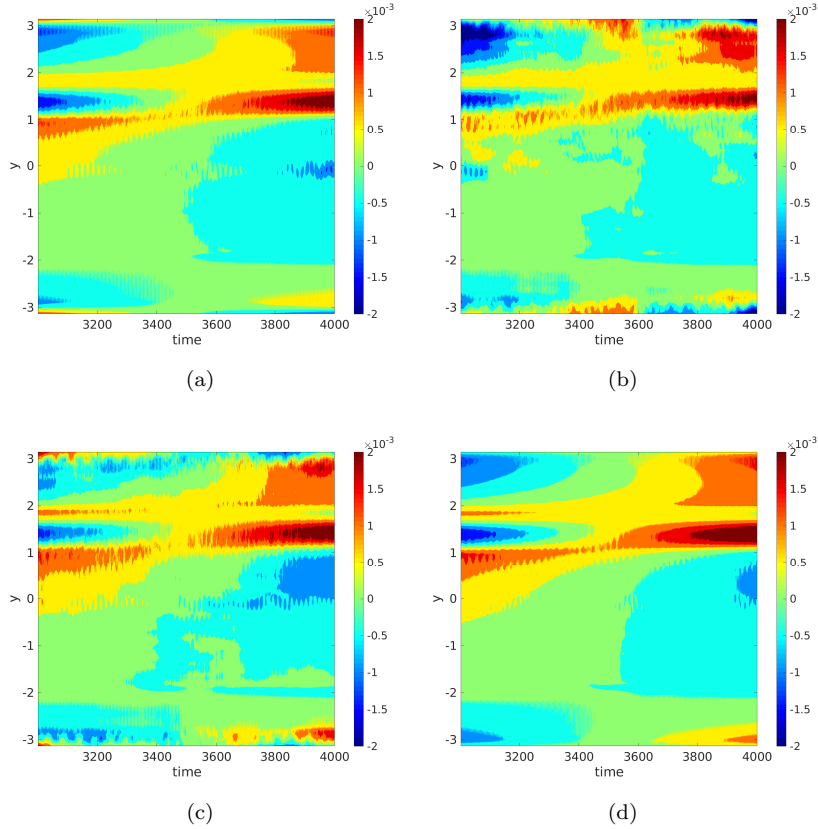


Figure 8. Time evolution of the barotropic EKE projected on the y -axis for the following cases: (a) deterministic low resolution simulation; (b) stochastic simulation with EOFs 1-2-3-4-5, $\Lambda \approx 0.47$; (c) DMD forced stochastic simulation $p = 2$, $m = 16$, $r = 7$, $\delta t = 0.1 \Delta t = 3\delta t$, $\Lambda \approx 0.47$; (d) reference solution.

434 5.4 Flow dynamics

435 In Figure 9 we show the time evolution of the projection over the zonal coordinate
 436 x of the barotropic potential vorticities for the time interval $t \in [1950, 2000]$. For a bet-
 437 ter comparison we removed the zonal mean and plot the resulting eddies. The projec-
 438 tion of the baroclinic PV displays similar results and is thus not discussed here. The same
 439 graph is shown for the low resolution deterministic simulation (Figure 9a), one realiza-
 440 tion with EOFs 1-2-3-4-5, $\Lambda \approx 0.47$ (Figure 9b), one with DMD $p = 2$, $m = 16$, $r =$

441 7, $\delta t = 0.1$, $\Delta t = 3\delta t$, $\Lambda \approx 0.47$ (Figure 9c), and for the reference solution (Figure
 442 9d). Although the eddy phase speed is correctly represented also by the low resolution
 443 simulation, the zonal extension and/or intensity of the eddies is underestimated; see for
 444 example around $t = 1965$ time units for $-3 < x < 0$. Both stochastic simulations
 445 maintain the correct eddy phase speed and help increasing the extension of the eddies,
 446 but DMD retains a stronger and less noisy signal. This result confirms the ability of DMD
 447 to include the sub-grid scales phenomena without weakening the signal of the larger scales.

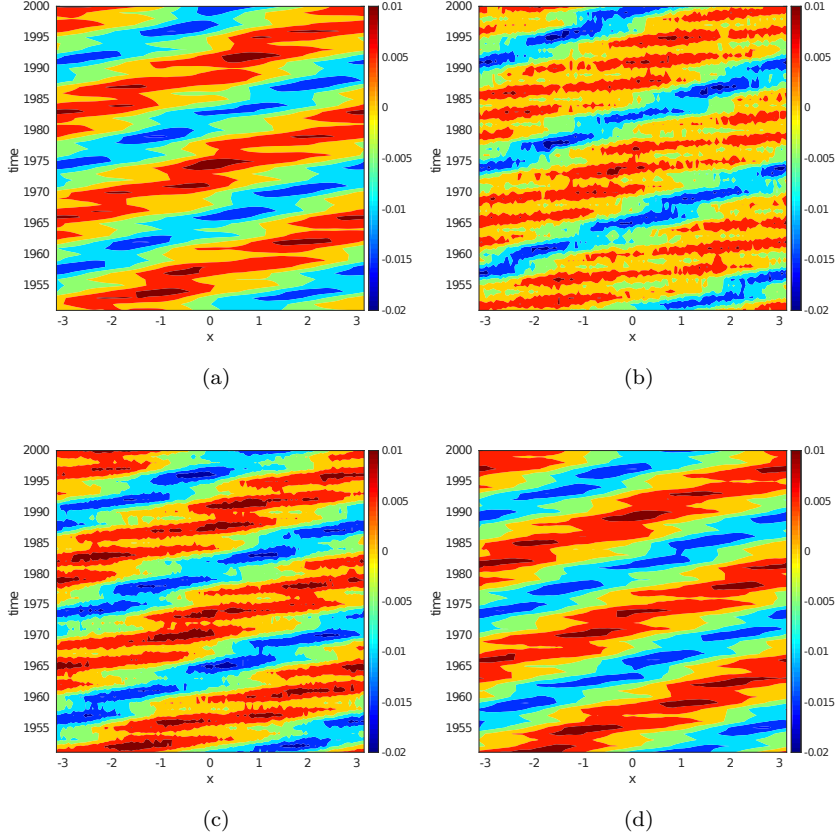


Figure 9. Time evolution in the interval $t \in [1950, 2000]$ of the barotropic PVs anomalies with respect to the zonal mean projected on the x -axis for the following cases: (a) deterministic low resolution simulation; (b) stochastic simulation with EOFs 1-2-3-4-5, $\Lambda \approx 0.47$; (c) DMD forced stochastic simulation $p = 2$, $m = 16$, $r = 7$, $\delta t = 0.1$ $\Delta t = 3\delta t$, $\Lambda \approx 0.47$; (d) reference solution.

448 6 Summary and discussion

449 In this study we develop a novel way to derive dynamically based noise covariance
 450 matrices which are flow-dependent. In the framework of the forced and damped 2-layer
 451 QG model we consider an energy-consistent stochastic parameterization based on the
 452 projection operator approach (Frank & Gottwald, 2013). As shown in Gugole and Franzke
 453 (2019), the definition of the noise spatial structure is of fundamental importance for this
 454 parameterization to return physically meaningful results, hence we analyze here two dif-
 455 ferent procedures for its definition. In particular, we investigate a statistical and a dy-
 456 namical approach by using two different dimension reduction techniques: Empirical Or-

457 orthogonal Functions and Dynamic Mode Decomposition. The former looks at the vari-
 458 ance field of the fluid, while the latter is strictly linked to the Koopman operator and
 459 hence to the generator of the dynamics. EOFs have been widely used in the literature,
 460 nevertheless there is in general no one-to-one correspondence between the EOF eigen-
 461 vectors and physical modes (von Storch & Zwiers, 2003). Moreover, being a statistical
 462 technique, it requires long time series in order to obtain reliable patterns. In contrast,
 463 DMD is able to work with *tall and skinny* matrices (Kutz et al., 2016), hence also with
 464 very short time series, and it has oscillatory modes. Therefore the choice of the length
 465 of the time series, $m\Delta t$, and the temporal shift between the two input matrices, δt , are
 466 crucial and serve as scale selection. In our model set-up we use half a eddy turn-over time
 467 as a physically based time interval to recompute the DMD. Since DMD decomposes the
 468 dynamics according to its local in time oscillatory behavior, its modes and the noise co-
 469 variance, have to be recomputed periodically. This is a new approach in stochastic pa-
 470 rameterizations allowing the noise covariance to be a function of time, while typically
 471 a fixed noise covariance is used during the whole realization.

472 Total energy graphs reveal that the EOF ensembles are either more dissipative or
 473 might include realizations with a clear increasing trend. On the other hand DMD runs
 474 are individually more energetically consistent with the high-resolution control simula-
 475 tion, suggesting that a dynamically adapted noise structure might help the model to stay
 476 on the manifold of constant energy. This might suggest that this approach may have the
 477 potential to lead to more dynamically consistent simulations and long-term stability. By
 478 analyzing the eddy kinetic energy, it has been discovered that in case of EOFs the un-
 479 certainties grow faster, which induce the single ensemble members to display very dif-
 480 ferent amplitudes of the EKE. Furthermore the location of the bi-modal structure of the
 481 EKE ensemble mean is not well defined among the individual realizations, and it is in
 482 general moved towards too high meridional locations. The DMD forced ensembles in-
 483 stead are able to follow the meridional jet shift and well catch the meridional location
 484 of the double-peak also at later times. Moreover the uncertainties grow more slowly, al-
 485 lowing the individual members to display a coherent behavior during the entire simu-
 486 lation and to stay close to the reference solution. Finally, the field dynamics time evo-
 487 lution in the DMD ensembles retain a stronger and less noisy signal.

488 As regards computational time, DMD is very cheap, can reliably deal with rather
 489 short time series and does not need extra computations beforehand, but can be run along-
 490 side the main code. These aspects allow the DMD algorithm to periodically reanalyze
 491 the dynamics and redefine the noise covariance accordingly. Hence it is a very good can-
 492 didate to parameterize scales undergoing phase transitions, or which do not reach sta-
 493 tistically stable profiles. This might also allow DMD to be used for scale-adaptive pa-
 494 rameterization schemes. Moreover, due to its close link to the Koopman operator, and
 495 to its ability to detect instabilities and bifurcations within dynamical systems (Bagheri,
 496 2013; Kutz et al., 2016), it might foster the system to reach tipping points or regime tran-
 497 sitions.

498 Our results suggest that a dynamically adapted spatial structure should be con-
 499 sidered in future developments of stochastic parameterizations. This is further motivated
 500 by the physics. Not only are the large scales affected by the small scales, but also the
 501 small-scale processes are influenced by the large-scale motions. Hence physically correct
 502 parameterizations of the unresolved scales should allow the sub-grid processes to be in-
 503 fluenced by the resolved modes. Furthermore, the propagation of the DMD modes by
 504 means of the Koopman operator might be seen as a sort of memory term, which in turn
 505 has been shown to be important in parameterization schemes (Franzke et al., 2015; Gottwald
 506 et al., 2017; Hu & Franzke, 2017; Sakradzija, Seifert, & Heus, 2015). However, more de-
 507 tailed studies are required to establish what kind of relation, if any, exists between the
 508 propagation of the DMD modes and memory terms.

509 **Acknowledgments**

510 This work is a contribution to the project M2 of the Collaborative Research Center TRR181
 511 *Energy Transfer in Atmosphere and Ocean* funded by the Deutsche Forschungsgemein-
 512 schaft (DFG, German Research Foundation) – Projektnummer 274762653. Model scripts
 513 are publicly available on GitHub[®]: https://github.com/FGugole/2L_QG_EOF_DMD. Data
 514 have been generated by use of the aforementioned scripts. The authors thank G. A. Gottwald
 515 and S. Juricke for discussions related to this work.

516 **References**

- 517 Arakawa, A. (1966). Computational design for long-term numerical integration of
 518 the equations of fluid motion: Two-dimensional incompressible flow. part i.
 519 *Journal of Computational Physics*, *1*(1), 119–143.
- 520 Badin, G., & Crisciani, F. (2018). *Variational formulation of fluid and geophys-*
 521 *ical fluid dynamics - mechanics, symmetries and conservation laws*. Springer
 522 Berlin.
- 523 Bagheri, S. (2013). Koopman-mode decomposition of the cylinder wake. *Journal of*
 524 *Fluid Mechanics*, *726*, 596623. doi: 10.1017/jfm.2013.249
- 525 Berloff, P. S. (2005). Random-forcing model of the mesoscale oceanic eddies. *Journal*
 526 *of Fluid Mechanics*, *529*, 7195. doi: 10.1017/S0022112005003393
- 527 Berner, J., Achatz, U., Batte, L., Bengtsson, L., Camara, A., Christensen, H., ...
 528 Yano, J. (2017). Stochastic parameterization: Toward a new view of weather
 529 and climate models. *Bull. Amer. Meteorol. Soc.*, *98*(3), 565–588.
- 530 Berner, J., Shutts, G., Leutbecher, M., & Palmer, T. (2009). A spectral stochastic
 531 kinetic energy backscatter scheme and its impact on flow-dependent pre-
 532 dictability in the ecmwf ensemble prediction system. *J. Atmos. Sci.*, *66*,
 533 603–626.
- 534 Budišić, M., Mohr, R., & Mezić, I. (2012). Applied Koopmanism. *Chaos: An*
 535 *Interdisciplinary Journal of Nonlinear Science*, *22*(4), 047510. Retrieved from
 536 <https://doi.org/10.1063/1.4772195> doi: 10.1063/1.4772195
- 537 Cotter, C. J., Crisan, D., Holm, D. D., Pan, W., & Shevchenko, I. (2018). Modelling
 538 uncertainty using circulation-preserving stochastic transport noise in a 2-layer
 539 quasi-geostrophic model. *arXiv:1802.05711*.
- 540 Cotter, C. J., Crisan, D., Holm, D. D., Pan, W., & Shevchenko, I. (2019). Numer-
 541 ically modelling stochastic Lie transport in fluid dynamics. *Multiscale Model.*
 542 *Simul.*, *17*, 192–232.
- 543 Cotter, C. J., Gottwald, G. A., & Holm, D. D. (2017). Stochastic partial dif-
 544 ferential fluid equations as a diffusive limit of deterministic lagrangian
 545 multi-time dynamics. *Proceedings of the Royal Society A: Mathematical,*
 546 *Physical and Engineering Sciences*, *473*(2205), 20170388. Retrieved from
 547 <https://royalsocietypublishing.org/doi/abs/10.1098/rspa.2017.0388>
 548 doi: 10.1098/rspa.2017.0388
- 549 Dubrulle, B. (2019). Beyond Kolmogorov cascades. *Journal of Fluid Mechanics*,
 550 *867*, P1. doi: 10.1017/jfm.2019.98
- 551 Dwivedi, S., Franzke, C. L. E., & Lunkeit, F. (2019). Energetically consistent
 552 stochastic and deterministic kinetic energy backscatter schemes for atmo-
 553 spheric models. *Q. J. Roy. Meteorol. Soc.*, *145*, 1–11.
- 554 Feldstein, S. B. (1998). An observational study of the intraseasonal poleward prop-
 555 agation of zonal mean flow anomalies. *Journal of the atmospheric sciences*,
 556 *55*(15), 2516–2529.
- 557 Frank, J. E., & Gottwald, G. A. (2013). Stochastic homogenization for an energy
 558 conserving multi-scale toy model of the atmosphere. *Physica D*, *254*, 46–56.
- 559 Franzke, C. L. E., Majda, A. J., & Vanden-Eijnden, E. (2005). Low-order stochas-
 560 tic mode reduction for a realistic barotropic model climate. *J. Atmos. Sci.*, *62*,
 561 1722–1745.

- 562 Franzke, C. L. E., O’Kane, T., Berner, J., Williams, P., & Lucarini, V. (2015).
 563 Stochastic climate theory and modelling. *WIREs Climate Change*, 6, 63–78.
- 564 Franzke, C. L. E., Oliver, M., Rademacher, J., & Badin, G. (2019). Systematic
 565 multi-scale methods for geophysical flows. In A. Iske & C. Eden (Eds.), *Energy*
 566 *transfers in atmosphere and ocean* (pp. 1–51). Springer.
- 567 Gardiner, C. W. (2009). *Stochastic methods: A handbook for the natural and social*
 568 *sciences* (Vol. 4). Springer Berlin.
- 569 Gavish, M., & Donoho, D. L. (2014, Aug). The optimal hard threshold for singular
 570 values is $4/\sqrt{3}$. *IEEE Transactions on Information Theory*, 60(8), 5040–5053.
 571 doi: 10.1109/TIT.2014.2323359
- 572 Gottwald, G., Crommelin, D., & Franzke, C. L. E. (2017). Stochastic climate theory.
 573 In C. L. E. Franzke & T. O’Kane (Eds.), *Nonlinear and stochastic climate*
 574 *dynamics* (pp. 209–240). Cambridge: Cambridge University Press.
- 575 Gugole, F., & Franzke, C. L. E. (2019). Numerical development and evaluation of an
 576 energy conserving conceptual stochastic climate model. *Mathematics for Cli-*
 577 *mate and Weather Forecasting*, 5, 45–64.
- 578 Hermanson, L., Hoskins, B., & Palmer, T. (2009). A comparative method to eval-
 579 uate and validate stochastic parametrizations. *Quarterly Journal of the Royal*
 580 *Meteorological Society: A journal of the atmospheric sciences, applied meteo-*
 581 *rology and physical oceanography*, 135(642), 1095–1103.
- 582 Holm, D. D. (2015). Variational principles for stochastic fluid dynamics. *Proc. R.*
 583 *Soc., A* 471, 20140963.
- 584 Holton, J. R. (2004). *An Introduction To Dynamic Meteorology* (Fourth Edi ed.).
- 585 Hu, G., & Franzke, C. L. E. (2017). Data assimilation in a multi-scale model. *Math-*
 586 *ematics of Climate and Weather Forecasting*, 3(1), 118–139.
- 587 Imkeller, P., & von Storch, J.-S. (Eds.). (2001). *Stochastic climate models* (Vol. 49).
 588 Basel: Birkhauser Verlag.
- 589 James, I., & Dodd, J. (1996). A mechanism for the low-frequency variability of the
 590 mid-latitude troposphere. *Quarterly Journal of the Royal Meteorological Soci-*
 591 *ety*, 122(533), 1197–1210.
- 592 Jansen, M. F., & Held, I. M. (2014). Parameterizing subgrid-scale eddy effects using
 593 energetically consistent backscatter. *Ocean Modelling*, 80, 36–48.
- 594 Jansen, M. F., Held, I. M., Adcroft, A., & Hallberg, R. (2015). Energy budget-based
 595 backscatter in an eddy permitting primitive equation model. *Ocean Modelling*,
 596 94, 15–26.
- 597 Jovanovic, M. R., Schmid, P. J., & Nichols, J. W. (2014). Sparsity-promoting dy-
 598 namic mode decomposition. *Physics of Fluids*, 26(2), 024103. Retrieved from
 599 <https://doi.org/10.1063/1.4863670> doi: 10.1063/1.4863670
- 600 Juricke, S., Danilov, S., Kutsenko, A., & Oliver, M. (2019). Ocean kinetic energy
 601 backscatter parametrizations on unstructured grids: Impact on mesoscale
 602 turbulence in a channel. *Ocean Modelling*, 138, 51 - 67. Retrieved from
 603 <http://www.sciencedirect.com/science/article/pii/S1463500318303846>
 604 doi: <https://doi.org/10.1016/j.ocemod.2019.03.009>
- 605 Kutz, J., Brunton, S., Brunton, B., & Proctor, J. (2016). *Dynamic mode decompo-*
 606 *sition*. Philadelphia, PA: Society for Industrial and Applied Mathematics. Re-
 607 trieved from <https://epubs.siam.org/doi/abs/10.1137/1.9781611974508>
 608 doi: 10.1137/1.9781611974508
- 609 Lasota, A., & Mackey, M. C. (1994). *Chaos, fractals and noise - stochastic aspects of*
 610 *dynamics*. Springer-Verlag.
- 611 Leith, C. (1996). Stochastic models of chaotic systems. *Physica D: Nonlinear Phe-*
 612 *nomena*, 98, 481–491.
- 613 Majda, A., Franzke, C. L. E., & Crommelin, D. (2009). Normal forms for reduced
 614 stochastic climate models. *Proc. Natl. Acad. Sci. USA*, 106, 3649–3653. doi:
 615 doi:10.1073/pnas.0900173106
- 616 Mémin, E. (2014). Fluid flow dynamics under location uncertainty. *Geophysical and*

- 617 *Astrophysical Fluid Dynamics*, 108, 119–46.
- 618 Mezić, I. (2013). Analysis of fluid flows via spectral properties of the Koopman
619 operator. *Annual Review of Fluid Mechanics*, 45(1), 357–378. Retrieved
620 from <https://doi.org/10.1146/annurev-fluid-011212-140652> doi:
621 10.1146/annurev-fluid-011212-140652
- 622 Noack, B. R., Stankiewicz, W., Morzyaski, M., & Schmid, P. J. (2016). Recursive
623 dynamic mode decomposition of transient and post-transient wake flows. *Jour-
624 nal of Fluid Mechanics*, 809, 843–872. doi: 10.1017/jfm.2016.678
- 625 Palmer, T., & Williams, P. (Eds.). (2010). *Stochastic physics and climate modelling*.
626 Cambridge: Cambridge University Press.
- 627 Pavliotis, G. A., & Stuart, A. (2008). *Multiscale methods: averaging and homoge-
628 nization*. Springer Science & Business Media.
- 629 Penland, C. (1989). Random forcing and forecasting using principal oscillation pat-
630 tern analysis. *Monthly Weather Review*, 117(10), 2165–2185. Retrieved from
631 [https://doi.org/10.1175/1520-0493\(1989\)117<2165:RFAFUP>2.0.CO;2](https://doi.org/10.1175/1520-0493(1989)117<2165:RFAFUP>2.0.CO;2)
632 doi: 10.1175/1520-0493(1989)117(2165:RFAFUP)2.0.CO;2
- 633 Penland, C., & Magorian, T. (1993). Prediction of nino 3 sea surface temperatures
634 using linear inverse modeling. *J. Climate*, 6(6), 1067–1076.
- 635 Porta Mana, P., & Zanna, L. (2014). Toward a stochastic parameterization of ocean
636 mesoscale eddies. *Ocean Modelling*, 79, 1–20.
- 637 Resseguier, V., Mémin, E., & Chapron, B. (2017a). Geophysical flows under lo-
638 cation uncertainty, part ii quasi-geostrophy and efficient ensemble spread-
639 ing. *Geophysical & Astrophysical Fluid Dynamics*, 111(3), 177–208. Re-
640 trieved from <https://doi.org/10.1080/03091929.2017.1312101> doi:
641 10.1080/03091929.2017.1312101
- 642 Resseguier, V., Mémin, E., & Chapron, B. (2017b). Geophysical flows under location
643 uncertainty, part i random transport and general models. *Geophysical & Astro-
644 physical Fluid Dynamics*, 111(3), 149–176. Retrieved from [https://doi.org/
645 10.1080/03091929.2017.1310210](https://doi.org/10.1080/03091929.2017.1310210) doi: doi:10.1080/03091929.2017.1310210
- 646 Resseguier, V., Pan, W., & Fox-Kemper, B. (2019). Data-driven versus self-similar
647 parameterizations for stochastic advection by Lie transport and location uncer-
648 tainty. *Nonlinear Processes in Geophysics Discussions*, 2019, 1–37. Retrieved
649 from [https://www.nonlin-processes-geophys-discuss.net/npg-2019-54/
650 doi: 10.5194/npg-2019-54](https://www.nonlin-processes-geophys-discuss.net/npg-2019-54/)
- 651 Riehl, H., Yeh, T., & La seur, N. E. (1950). A study of variations of the general cir-
652 culation. *Journal of Meteorology*, 7(3), 181–194.
- 653 Rowley, C. W., Mezić, I., Bagheri, S., Schlatter, P., & Henningson, D. S. (2009).
654 Spectral analysis of nonlinear flows. *J. Fluid Mech.*, 641, 115–127. Re-
655 trieved from <https://doi.org/10.1017/S0022112009992059> doi:
656 10.1017/S0022112009992059
- 657 Sakradzija, M., Seifert, A., & Heus, T. (2015). Fluctuations in a quasi-stationary
658 shallow cumulus cloud ensemble. *Nonlin. Proc. Geophys.*, 22(1), 65–85.
- 659 Salmon, R. (1988). Hamiltonian fluid mechanics. *Annual Review of Fluid Me-
660 chanics*, 20(1), 225–256. Retrieved from [https://doi.org/10.1146/annurev
661 .fl.20.010188.001301](https://doi.org/10.1146/annurev.fl.20.010188.001301) doi: 10.1146/annurev.fl.20.010188.001301
- 662 Sardeshmukh, P. D., & Sura, P. (2009). Reconciling non-gaussian climate statistics
663 with linear dynamics. *J. Climate*, 22(5), 1193–1207.
- 664 Schmid, P. J. (2010). Dynamic mode decomposition of numerical and experimental
665 data. *Journal of Fluid Mechanics*, 656, 528. doi: 10.1017/S0022112010001217
- 666 Schmid, P. J., Li, L., Juniper, M. P., & Pust, O. (2011, Jun 01). Applications of the
667 dynamic mode decomposition. *Theoretical and Computational Fluid Dynamics*,
668 25(1), 249–259. Retrieved from [https://doi.org/10.1007/s00162-010-0203
669 -9](https://doi.org/10.1007/s00162-010-0203-9) doi: 10.1007/s00162-010-0203-9
- 670 Schmid, P. J., Meyer, K. E., & Pust, O. (2009). Dynamic mode decomposition and
671 proper orthogonal decomposition of flow in a lid-driven cylindrical cavity. In

- 672 *8th international symposium on particle image velocimetry – PIV09.*
673 Shepherd, T. G. (1990). Symmetries, conservation laws, and Hamiltonian structure
674 in geophysical fluid dynamics. *Advances in Geophysics*, 32, 287–338.
675 Stensrud, D. J. (2007). *Parameterization schemes*. Cambridge University Press.
676 Tu, J. H., Rowley, C. W., Luchtenburg, D. M., Brunton, S. L., & Kutz, J. N.
677 (2014). On dynamic mode decomposition: Theory and applications.
678 *Journal of Computational Dynamics*, 1, 391. Retrieved from [http://](http://aimsciences.org//article/id/1dfebc20-876d-4da7-8034-7cd3c7ae1161)
679 aimsciences.org//article/id/1dfebc20-876d-4da7-8034-7cd3c7ae1161
680 doi: 10.3934/jcd.2014.1.391
681 Vallis, G. K. (2006). *Atmospheric and oceanic fluid dynamics: fundamentals and*
682 *large-scale circulation*. Cambridge University Press.
683 von Storch, H. (1995). Spatial patterns: Eofs and cca. In H. von Storch &
684 A. Navarra (Eds.), *Analysis of climate variability: Applications of statistical*
685 *techniques* (pp. 227–257). Berlin, Heidelberg: Springer Berlin Heidelberg.
686 Retrieved from https://doi.org/10.1007/978-3-662-03167-4_13 doi:
687 10.1007/978-3-662-03167-4_13
688 von Storch, H., & Zwiers, F. W. (2003). *Statistical analysis in climate research*.
689 Cambridge University Press.
690 Whitaker, J. S., & Sardeshmukh, P. D. (1998). A linear theory of extratropical syn-
691 optic eddy statistics. *J. Atmos. Sci.*, 55(2), 237–258.
692 Williams, M. O., Kevrekidis, I. G., & Rowley, C. W. (2015). A data-driven approx-
693 imation of the Koopman operator: extending dynamic mode decomposition. *J.*
694 *Nonlinear Sci.*, 25(6), 1307–1346. Retrieved from [https://doi.org/10.1007/](https://doi.org/10.1007/s00332-015-9258-5)
695 [s00332-015-9258-5](https://doi.org/10.1007/s00332-015-9258-5) doi: 10.1007/s00332-015-9258-5
696 Zhang, Y., & Held, I. M. (1999). A linear stochastic model of a gcms midlatitude
697 storm tracks. *J. Atmos. Sci.*, 56(19), 3416–3435.
698 Zurita-Gotor, P., Held, I. M., & Jansen, M. F. (2015). Kinetic energy-conserving
699 hyperdiffusion can improve low resolution atmospheric models. *J. Adv. Mol.*
700 *Earth Sys.*, 7(3), 1117–1135.